Inorg. Chem. **2006**, *45*, 10188–10196

En Route to the Formation of High-Efficiency, Osmium(II)-Based Phosphorescent Materials

Fang-Chi Hsu, Yung-Liang Tung, and Yun Chi*

Department of Chemistry, National Tsing Hua University, Hsinchu 300, Taiwan

Cheng-Chih Hsu, Yi-Ming Cheng, Mei-Lin Ho, Pi-Tai Chou,* and Shie-Ming Peng

Department of Chemistry and Instrumentation Center, National Taiwan University, Taipei 106, Taiwan

Arthur J. Carty*

Steacie Institute for Molecular Sciences, National Research Council Canada, 100 Sussex Drive, Ottawa, Ontario K1A 0R6, Canada

Received July 14, 2006

Triosmium cluster complexes $[Os_3(CO)_8(fppz)_2]$ (**2a**) and $[Os_3(CO)_8(fptz)_2]$ (**2b**) bearing two 2-pyridyl azolate ligands were synthesized in an attempt to establish the reaction mechanism that gives rise to the blue-emitting phosphorescent complexes $[Os(CO)_2(fppz)_2]$ (**1a**) and $[Os(CO)_2(fptz)_2]$ (**1b**) [(fppz)H = 3-(trifluoromethyl)-5-(2-pyridyl)pyrazole; (fptz)H = 3-(trifluoromethyl)-5-(2-pyridyl)triazole]. X-ray structural analysis of **2b** showed an open triangular metal framework incorporating multisite-coordinated 2-pyridyltriazolate ligands. Treatment of **2** with the respective 2-pyridylazolate ligand led to the formation of blue-emitting complex **1b**, confirming their intermediacy, while the reaction of **2b** with phosphine ligand PPh_2Me afforded two hitherto novel hydride complexes **3** and **4**, for which the reversible interconversion was clearly established at higher temperatures (>180 °C). The single-crystal X-ray diffraction analyses of **3** and **4** confirmed their monometallic and isomeric nature, together with the coordination of two phosphine ligands located in the trans-disposition and one CO and one hydride located opposite to the pyridyl triazolate chelate. Subtle differences in photophysical properties were examined for isomers **3** and **4** on the basis of steady state absorption and emission, the relaxation dynamics, and temperature-dependent luminescent studies. The results, in combination with time-dependent density function theory (TDDFT) calculations, provide fundamental insights into the future design and preparation of highly efficient phosphorescent emitters.

Introduction

The third-row transition metal complexes have been extensively utilized for the fabrication of phosphorescent organic light-emitting diodes (OLEDs).[1] The imposed strong spin−orbit coupling effectively promotes singlet-to-triplet intersystem crossing and enhances the subsequent radiative transition from the triplet state to the ground state. Because an internal phosphorescence quantum efficiency (η_{int}) of as high as ∼100% could theoretically be achieved, these heavy metal containing emitters, which are capable of harnessing both singlet and triplet excitons, should be superior to their fluorescent counterparts in giving higher device efficiencies.[2] As a result, research activities are shifting focus from traditional fluorescent dyes to the exploration of heavy transition metal-based phosphorescent emitters, particularly for those metal complexes that possess good thermal and

* To whom correspondence should be addressed. E-mail: ychi@mx.nthu.edu.tw (Y.C.), chop@ntu.edu.tw (P.-T.C.), acarty@pco-bcp.gc.ca (A.J.C.).

(1) (a) Holder, E.; Langeveld, B. M. W.; Schubert, U. S. *Adv. Mater.* **2005**, *17*, 1109. (b) Yersin, H. *Top. Curr. Chem.* **2004**, *241*, 1. (c) Welter, S.; Brunner, K.; Hofstraat, J. W.; De Cola, L. *Nature (London)* **2003**, *421*, 54. (d) Sun, Y.; Giebink, N. C.; Kanno, H.; Ma, B.; Thompson, M. E.; Forrest, S. R. *Nature* **2006**, *440*, 908. (e) Chou, P.-T.; Chi, Y. *Eur. J. Inorg. Chem.* **2006**, 3319.

(2) (a) Adachi, C.; Baldo, M. A.; Thompson, M. E.; Forrest, S. R. *J. Appl. Phys.* **2001**, *90*, 5048. (b) Kawamura, Y.; Goushi, K.; Brooks, J.; Brown, J. J.; Sasabe, H.; Adachi, C. *Appl. Phys. Lett.* **2005**, *86*, 071104.

10.1021/ic061301y CCC: $33.50
Published on Web 11/04/2006

electrochemical stability, better RGB chromaticity, and superior luminescent quantum efficiency upon excitation.

With respect to complexes exhibiting phosphorescence at room temperature, most investigations have been focusing on the d^6 and d^8 transition metal complexes.[3] The luminescent platinum(II) d^8 metal complexes, however, due to their planar molecular geometry, may induce significant intermolecular interaction in the solid state resulting in difficulties in assessing their photophysical properties and hence the device performance.[4] On the other hand, both homoleptic and/or heteroleptic coordination architectures of d^6 iridium(III) complexes have been extensively studied, showing an elegant interplay between the photophysical properties and the coordinated chromophores.[5] In particular, octahedral iridium(III) systems with at least two cyclometalating chromophores have shown much more predictable behavior for fabricating light-emitting devices.[6] As a result, versatile ligand designs can be applied to tune excited-state properties such as emission energy gap, lifetime, and quantum yield.

In yet another approach, to explore the versatility of the octahedral osmium(II) complexes, we have prepared several luminous complexes with formulas $[OsI_2(CO)_2(\text{diimine})]$ (diimine = bipyridine or phenanthroline)[7] and $[OsX(CO)_3(\text{chelate})]$ (X = halide or pseudohalide; chelate is, for example, a substituted β-diketonate[8] or quinolinolate anion).[9] Three representative structural drawings are depicted in Chart 1, for which the accompanying studies have clearly unraveled the nature of the excited states that gave the bright phosphorescence at room temperature. In this paper, we present a comprehensive approach to extend the previously documented reactions involving pyridylazoles (denoted as N∧NH) and osmium carbonyl reagent $Os_3(CO)_{12}$.[1e,10] Attention is paid to several distinctive issues such as possible mechanistic pathways and how to broaden reactivity patterns using newly isolated intermediates.

Chart 1

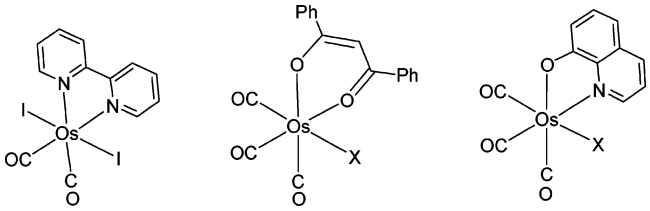

Experimental Section

General Information and Materials. All reactions were performed under a nitrogen atmosphere using anhydrous solvents or solvents treated with an appropriate drying reagent. Mass spectra were obtained on a JEOL SX-102A instrument operating in electron impact (EI) mode or fast atom bombardment (FAB) mode. ^{1}H and ^{19}F NMR spectra were recorded on a Varian Mercury-400 or INOVA-500 instrument. Elemental analyses were conducted at the NSC Regional Instrumentation Center at National Chiao Tung University. The nitrogen chelates, 3-(trifluoromethyl)-5-(2-pyridyl)-pyrazole, (fppz)H, and 3-(trifluoromethyl)-5-(2-pyridyl)triazole, (fptz)H, were prepared using methods reported in the literature.[11]

Preparation of 2a. A mixture of $Os_3(CO)_{12}$ (200 mg, 0.22 mmol) and fppzH (141 mg, 0.66 mmol) in 25 mL of anhydrous diethylene glycol monoethyl ether (DGME) was heated at 180 °C for 12 h. After being cooled to room temperature, the solvent was removed under vacuum and the residue purified using silica gel column chromatography, eluting with a mixture of ethyl acetate (EA) and hexane (1:1). A yellow crystalline sample of $[Os_3(CO)_8(fppz)_2]$ was obtained from CH_2Cl_2 and methanol at room temperature; yield 72% (193 mg, 0.16 mmol).

Spectral data for **2a**: MS (FAB, ^{192}Os) *m*/*z* 1224 (M^+); IR (C_6H_{12}) ν(CO), 2079 (s), 2012 (vs), 1996 (vs), 1970 (w), 1944 (s) cm^{-1}; ^{1}H NMR (500 MHz, acetone-d_6, 294 K) δ 9.25 (d, 1H, J_{HH} = 5.0 Hz), 8.16 (td, 1H, J_{HH} = 8.0, 1.0 Hz), 8.04 (d, 1H, J_{HH} = 8.0 Hz), 7.64 (ddd, 1H, J_{HH} = 6.3, 6.0, 1.5 Hz), 7.14 (s, 1H); ^{19}F NMR (470 MHz, acetone-d_6) δ −57.5 (s). Anal. Calcd for $C_{26}H_{10}F_6N_6O_8Os_3$: C, 25.62; N, 6.98; H, 0.83. Found: C, 25.87; N, 6.84; H, 0.81.

Preparation of 2b. Similar to the procedure described for **2a**, this product was prepared using $Os_3(CO)_{12}$ (200 mg, 0.22 mmol) and fptzH (142 mg, 0.66 mmol). Yellow crystals of $[Os_3(CO)_8(fptz)_2]$ were obtained by recrystallization from a mixture of CH_2Cl_2 and methanol; yield 60% (161 mg, 0.13 mmol).

Spectral data for **2b**: MS (FAB, ^{192}Os) *m*/*z* 1226 (M^+); IR (C_6H_{12}) ν(CO), 2083 (w), 2015 (vs), 2000 (s), 1976 (w), 1949 cm^{-1}; ^{1}H NMR (500 MHz, acetone-d_6, 294 K) δ 9.39 (d, 1H, J_{HH} = 5.5 Hz), 8.32 (td, 1H, J_{HH} = 8.0, 1.5 Hz), 8.11 (d, 1H, J_{HH} = 8.0 Hz), 7.88 (ddd, 1H, J_{HH} = 6.3, 5.5, 1.5 Hz); ^{19}F NMR (470 MHz,

(3) (a) Vogler, A.; Kunkely, H. *Top. Curr. Chem.* **2001**, *213*, 143. (b) Welter, S.; Salluce, N.; Belser, P.; Groeneveld, M.; De Cola, L. *Coord. Chem. Rev.* **2005**, *249*, 1360. (c) Browne, W. R.; O'Boyle, N. M.; McGarvey, J. J.; Vos, J. G. *Chem. Soc. Rev.* **2005**, *34*, 641.
(4) (a) Lai, S.-W.; Che, C.-M. *Top. Curr. Chem.* **2004**, *241*, 27. (b) Ma, B.; Li, J.; Djurovich, P. I.; Yousufuddin, M.; Bau, R.; Thompson, M. E. *J. Am. Chem. Soc.* **2005**, *127*, 28. (c) Lu, W.; Chan, M. C. W.; Zhu, N.; Che, C.-M.; Li, C.; Hui, Z. *J. Am. Chem. Soc.* **2004**, *126*, 7639. (d) Kavitha, J.; Chang, S.-Y.; Chi, Y.; Yu, J.-K.; Hu, Y.-H.; Chou, P.-T.; Peng, S.-M.; Lee, G.-H.; Tao, Y.-T.; Chien, C.-H.; Carty, A. J. *Adv. Funct. Mater.* **2005**, *15*, 223. (e) Chang, S.-Y.; Kavitha, J.; Li, S.-W.; Hsu, C.-S.; Chi, Y.; Yeh, Y.-S.; Chou, P.-T.; Lee, G.-H.; Carty, A. J.; Tao, Y.-T.; Chien, C.-H. *Inorg. Chem.* **2006**, *45*, 137.
(5) (a) Li, J.; Djurovich, P. I.; Alleyne, B. D.; Yousufuddin, M.; Ho, N. N.; Thomas, J. C.; Peters, J. C.; Bau, R.; Thompson, M. E. *Inorg. Chem.* **2005**, *44*, 1713. (b) Sajoto, T.; Djurovich, P. I.; Tamayo, A.; Yousufuddin, M.; Bau, R.; Thompson, M. E.; Holmes, R. J.; Forrest, S. R. *Inorg. Chem.* **2005**, *44*, 7992. (c) Yang, C.-H.; Li, S.-W.; Chi, Y.; Cheng, Y.-M.; Yeh, Y.-S.; Chou, P.-T.; Lee, G.-H.; Wang, C.-H.; Shu, C.-F. *Inorg. Chem.* **2005**, *44*, 7770.
(6) (a) Hwang, F.-M.; Chen, H.-Y.; Chen, P.-S.; Liu, C.-S.; Chi, Y.; Shu, C.-F.; Wu, F.-I.; Chou, P.-T.; Peng, S.-M.; Lee, G.-H. *Inorg. Chem.* **2005**, *44*, 1344. (b) You, Y.; Park, S. Y. *J. Am. Chem. Soc.* **2005**, *127*, 12438.
(7) Chen, Y.-L.; Lee, S.-W.; Chi, Y.; Hwang, K.-C.; Kumar, S. B.; Hu, Y.-H.; Cheng, Y.-M.; Chou, P.-T.; Peng, S.-M.; Lee, G.-H.; Yeh, S.-J.; Chen, C.-T. *Inorg. Chem.* **2005**, *44*, 4287.
(8) (a) Chen, Y.-L.; Sinha, C.; Chen, I.-C.; Liu, K.-L.; Chi, Y.; Yu, J.-K.; Chou, P.-T.; Lu, T.-H. *Chem. Commun.* **2003**, 3046. (b) Chen, Y.-L.; Li, S.-W.; Chi, Y.; Cheng, Y.-M.; Pu, S.-C.; Yeh, Y.-S.; Chou, P.-T. *ChemPhysChem* **2005**, *6*, 2012.
(9) Cheng, Y.-M.; Yeh, Y.-S.; Ho, M.-L.; Chou, P.-T.; Chen, P.-S.; Chi, Y. *Inorg. Chem.* **2005**, *44*, 4594.
(10) (a) Wu, P.-C.; Yu, J.-K.; Song, Y.-H.; Chi, Y.; Chou, P.-T.; Peng, S.-M.; Lee, G.-H. *Organometallics* **2003**, *22*, 4938. (b) Yu, J.-K.; Hu, Y.-H.; Cheng, Y.-M.; Chou, P.-T.; Peng, S.-M.; Lee, G.-H.; Carty, A. J.; Tung, Y.-L.; Lee, S.-W.; Chi, Y.; Liu, C.-S. *Chem.*—Eur. J. **2004**, *10*, 6255.
(11) (a) Yu, W.-S.; Cheng, C.-C.; Cheng, Y.-M.; Wu, P.-C.; Song, Y.-H.; Chi, Y.; Chou, P.-T. *J. Am. Chem. Soc.* **2003**, *125*, 10800. (b) Cheng, C.-C.; Yu, W.-S.; Chou, P.-T.; Peng, S.-M.; Lee, G.-H.; Wu, P.-C.; Song, Y.-H.; Chi, Y. *Chem. Commun.* **2003**, 2628. (c) Klingele, M. H.; Brooker, S. *Coord. Chem. Rev.* **2003**, *241*, 119.

Table 1. Crystal Data and Structure Refinement Parameters for Complexes **2b**, **3**, and **4**

param	**2b**	**3**	**4**
empirical formula	$C_{24}H_8F_6N_8O_8Os_3$	$C_{35}H_{31}F_3N_4OOsP_2$	$C_{35}H_{31}F_3N_4OOsP_2{\cdot}1/2CH_2Cl_2$
fw	1220.98	832.78	875.24
temp (K)	295(2)	295(2)	150(1)
cryst system	monoclinic	monoclinic	monoclinic
space group	$P2_1/c$	$P2_1/c$	$P2_1/n$
a (Å)	16.9045(8)	11.1450(5)	10.2530(4)
b (Å)	13.6895(7)	32.2482(14)	15.8852(6)
c (Å)	12.7028(6)	9.5374(4)	20.9409(8)
β (deg)	93.774(1)	90.0610(10)	90.366(1)
V (Å^3), Z	2933.2(2), 4	3427.8(3), 4	3410.6(2), 4
d(calcd) (Mg/m^3)	2.765	1.614	1.705
abs coeff (mm^{-1})	13.065	3.863	3.963
F(000)	2216	1640	1724
cryst size (mm^3)	0.28 × 0.20 × 0.20	0.23 × 0.14 × 0.06	0.30 × 0.15 × 0.10
reflcns collcd	28854	27933	33813
indepdt reflcns	6738 [R(int) = 0.0503]	6045 [R(int) = 0.0631]	7854 [R(int) = 0.0593]
max and min transm	0.1798 and 0.1209	0.8013 and 0.4702	0.6927 and 0.3827
data/restraints/params	6738/0/452	6045/0/448	7845/1/514
goodness-of-fit on F^2	1.027	1.189	1.020
final R indices [$I > 2\sigma(I)$]	$R_1 = 0.0329$, $wR_2 = 0.0679$	$R_1 = 0.0562$, $wR_2 = 0.1035$	$R_1 = 0.0364$, $wR_2 = 0.0773$
R indices (all data)	$R_1 = 0.0425$, $wR_2 = 0.0716$	$R_1 = 0.0703$, $wR_2 = 0.1083$	$R_1 = 0.0491$, $wR_2 = 0.0823$
largest diff peak and hole (e Å^{-3})	1.363 and −1.075	1.378 and −2.394	1.574 and −1.781

acetone-d_6) δ −61.8 (s). Anal. Calcd for $C_{24}H_8F_6N_8O_8Os_3$: C, 23.61; N, 9.18; H, 0.66. Found: C, 23.75; N, 9.27; H, 1.01.

Reaction of 2a with fppzH and 2b with fptzH. A mixture of **2a** (100 mg, 0.08 mmol) and fppzH (78.7 mg, 0.36 mmol) in10 mL of DGME was heated at 190 °C for 24 h. Solvent was removed under vacuum, and the residue was separated using silica gel column chromatography (ethyl acetate), giving 64 mg of recovered **2a** (0.052 mmol, 64%) together with blue-emitting **1a** [$Os(CO)_2(fppz)_2$] (51 mg, 0.075 mmol, 31%). Similarly, complex **2b** reacted with fptzH to afford **1b** and unreacted **2b** in 35% and 60% of yields, respectively.

Reaction of 2b with PPh_2Me. A mixture of **2b** (200 mg, 0.16 mmol) and PPh_2Me (183 μL, 0.98 mmol) in 25 mL of DGME was heated at 180 °C for 12 h. After being cooled to room temperature, the solvent was removed and the residue was separated using silica gel column chromatography (1:1 ethyl acetate/hexane), giving a blue-emitting complex **3** (75 mg, 0.09 mmol, 55%) together with a green-emitting complex **4** (14 mg, 0.016 mmol, 10%) according to the sequence of their elution. Single crystals of **3** and **4** were obtained by recrystallization from a mixture of EA/hexane and CH_2Cl_2/hexane, respectively.

Spectral data for **3**: MS (FAB, ^{192}Os) m/z 834 (M^+), 634 ($M^+ - PPh_2Me$); IR (CH_2Cl_2) ν(Os−H), 2053 (w), ν(CO), 1912 (vs) cm^{-1}; ^{1}H NMR (500 MHz, acetone-d_6, 294 K) δ 8.14 (d, 1H, J_{HH} = 5.0 Hz), 7.62 (t, 1H, J_{HH} = 7.5 Hz), 7.43 (d, 1H, J_{HH} = 7.5 Hz), 7.39−7.35 (m, 4H), 7.32−7.29 (m, 2H), 7.25−7.19 (m, 14H), 6.85 (t, 1H, J_{HH} = 6.5 Hz), 1.71 (t, 6H, J_{HP} = 3.0 Hz, CH_3), −12.77 (t, 1H, J_{HP} = 18.5 Hz); ^{31}P NMR (202 MHz, acetone-d_6) δ 0.73 (s); ^{19}F NMR (470 MHz, acetone-d_6) δ −62.7 (s). Anal. Calcd for $C_{35}H_{31}F_3N_4OOsP_2$: C, 50.48; N, 6.73; H, 3.75. Found: C, 50.52; N, 6.79; H, 3.81.

Spectral data for **4**: MS (FAB, ^{192}Os) m/z 834 (M^+), 634 ($M^+ - PPh_2Me$); IR (CH_2Cl_2) ν(Os−H), 2016 (w), ν(CO), 1937 (vs) cm^{-1}; ^{1}H NMR (500 MHz, acetone-d_6, 294 K) δ 7.94 (d, 1H, J_{HH} = 5.5 Hz), 7.49 (d, 1H, J_{HH} = 7.5 Hz), 7.42−7.40 (m, 4H), 7.33−7.28 (m, 3H), 7.23−7.20 (m, 4H), 7.19−7.17 (m, 2H), 7.13−7.08 (m, 8H) 6.53 (ddd, 1H, J_{HH} = 6.3, 5.5, 1.5 Hz), 2.06 (t, 6H, J_{HP} = 3.5 Hz, Me), −12.28 (t, 1H, J_{HP} = 18.0 Hz); ^{31}P NMR (202 MHz, acetone-d_6) δ −0.57 (s); ^{19}F NMR (470 MHz, acetone-d_6) δ −62.4 (s). Anal. Calcd for $C_{35}H_{31}F_3N_4OOsP_2$: C, 50.48; N, 6.73; H, 3.75. Found: C, 50.47; N, 6.78; H, 3.96.

Isomerization of 3. A DGME solution of **3** (20 mg, 0.024 mmol) was heated at 180 °C for 24 h. After being cooled to room temperature, the solvent was removed under vacuum and the residue was separated using silica gel column chromatography (1:1 ethyl acetate/hexane), giving 10 mg of recovered **3** (0.012 mmol, 50%) and 5.0 mg of **4** (0.006 mmol, 25%).

Isomerization of 4. A DGME solution of **4** (20 mg, 0.024 mmol) was heated at 180 °C for 24 h. After being cooled to room temperature, the solvent was removed under vacuum and the solid residue was separated using silica gel column chromatography (1:1 ethyl acetate/hexane), giving 4.0 mg of **3** (0.005 mmol, 20%) and 9.6 mg of unreacted **4** (0.012 mmol, 48%). Note that from a thermodynamic viewpoint, the same ratio should be expected for both forward (**3** → **4**) and reverse reactions (**4** → **3**). Unfortunately, reversibility is not sufficient due to certain sample decomposition during heating. Accordingly, only qualitative results were reported here.

X-ray Structural Determination. Single-crystal X-ray diffraction data were recorded on a Bruker SMART CCD diffractometer using λ(Mo Kα) radiation (λ = 0.710 73 Å). The data collection was executed using the SMART program. Cell refinement and data reduction were made with the SAINT program. The structure was determined using the SHELXTL/PC program and refined using full-matrix least squares. All non-hydrogen atoms were refined anisotropically, whereas hydrogen atoms were placed at the calculated positions and included in the final stage of refinements with fixed positional parameters. The crystallographic refinement parameters of complexes **2b**, **3**, and **4** are summarized in Table 1, while the selective bond distances and angles of these complexes are listed in Tables 2−4, respectively.

Spectral Measurement. Steady-state absorption and emission spectra were recorded with a Hitachi (U-3310) spectrophotometer and an Edinburgh (FS920) fluorometer, respectively. Quinine sulfate with an emission yield of $\Phi \sim 0.55$ ($\lambda_{max} \sim 460$ nm) in 0.1 M H_2SO_4 served as a standard to calculate the emission quantum yield.[12] Lifetime studies were performed with an Edinburgh FL 900 photon-counting system with a hydrogen-filled/or a nitrogen lamp as the excitation source. Data were analyzed using the nonlinear least-squares procedure in combination with an iterative

(12) Demas, J. N.; Crosby, G. A. *J. Phys. Chem.* **1971**, *75*, 991.

convolution method. The emission decays were analyzed by the sum of exponential functions, which allows partial removal of the instrument time broadening and consequently renders a temporal resolution of ~200 ps.

Computational Methodology. Time-dependent DFT calculations based on the geometry taken from the X-ray analyses of complexes **3** and **4** were carried out using a hybrid B3LYP method,[13] while a double-ζ quality basis set consisting of Hay and Wadt's effective core potentials (LANL2DZ)[14] was employed for osmium atoms; a 6-31G(d′,p′) basis set was employed for the H, C, N, F, P, and O atoms. A relativistic effective core potential (ECP) replaced the inner core electrons of Os(II), leaving the outer core ($5s^25p^6$) electrons and the $5d^6$ valence electrons. Typically, the lowest triplet and singlet roots of the nonhermitian eigenvalue equations were obtained to determine the vertical excitation energies. Oscillator strengths were deduced from the dipole transition matrix elements (for singlet states only). The excited-state TDDFT calculations were carried out using Gaussian03.[15]

Results

Synthesis and Characterization. It has been reported that the simplest and most straightforward synthetic route to the blue-emitting osmium(II) complexes **1a**,**b** involves the direct treatment of $Os_3(CO)_{12}$ with at least 6 equiv of pyridylazole chelate (denoted as N∧NH) in a high boiling alcohol solvent DGME (Scheme 1).[10] The reaction possibly proceeds through a multistep process, involving the prior formation of mononuclear intermediates such as $Os(CO)_x$, $4 \leq x \leq 2$, followed by addition of N∧NH ligands, CO dissociation, and the removal of an activated hydrogen atom on the N∧N chelate. However, due to the stronger Os−Os bonding interaction, the simultaneous cleavage of all three Os−Os bonds of $Os_3(CO)_{12}$ in forming the intermediate $Os(CO)_x$ would require excess thermal energy and become exceedingly difficult. This leads us to believe that the dissociation of the Os−Os bonds should occur in a stepwise manner during the reaction. Such a proposed mechanism prompted us to conduct the reaction employing a reduced amount of the N∧NH ligand in an attempt to isolate the possible reaction intermediates.

A remarkable contrast was immediately observed upon changing the molar ratio of $Os_3(CO)_{12}$ and pyridyl pyrazolate

Scheme 1

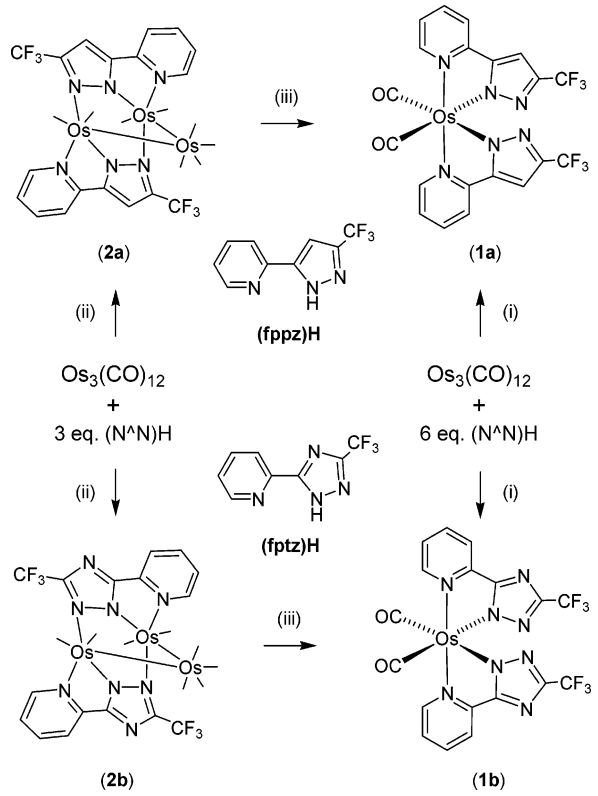

fppzH from 1:6 to 1:3, leading to the formation of a distinctive yellow complex $[Os_3(CO)_8(fppz)_2]$ (**2a**) in 72% yield, together with only trace amounts of the original blue-emitting product $[Os(CO)_2(fppz)_2]$ (**1a**). A similar transformation was observed when $Os_3(CO)_{12}$ was treated with 3 equiv of pyridyltriazole fptzH under similar conditions, giving the analogous cluster complex $[Os_3(CO)_8(fptz)_2]$ (**2b**) in a slightly lower yield (60%). The FAB mass spectrometry of the azolate complexes **2a**,**b** revealed the molecular ion (M^+) signals at $m/z = 1224$ and 1226, providing clear evidence for the incorporation of two fppz (or fptz) ligands into the triosmium framework, together with the retention of eight ancillary carbonyl ligands. In good agreement with this prediction, the IR spectra of both **2a**,**b** in CH_2Cl_2 showed five sharp ν(CO) absorptions in the range 2083−1944 cm^{-1}, confirming the multimetallic cluster nature, while the simplified ^1H and ^{19}F NMR spectral pattern revealed the existence of two magnetically equivalent N∧N chelates due to the inherent C_2 symmetry of the complexes.

An X-ray diffraction study of triazolate complex **2b** was then carried out to further confirm the structural identities of these molecules. As presented in Figure 1, three osmium atoms are linked in an open triangular geometry with Os−Os distances being 2.8401(4) and 2.8440(4) Å, which deviate only slightly from the average value in parent compound $Os_3(CO)_{12}$ (2.877 Å).[16] The through-space contact between the nonbonded osmium atoms is notably longer, 3.771(1) Å, which is even longer than that (3.078 Å) observed in the open triangular alkoxide cluster complex $[Os_3(CO)_{10}(\mu\text{-}OMe)_2]$, for which the nonbonding interaction is consistent

(13) (a) Becke, A. D. *J. Chem. Phys.* **1993**, *98*, 5648. (b) Lee, C.; Yang, W.; Parr, R. G. *Phys. Rev. B* **1988**, *37*, 785.

(14) (a) Dunning, T. H.; Hay, P. J. *In Modern Theoretical Chemistry*; Schaefer, H. F., III, Ed.; Plenum Press: New York, 1976; Vol. 3, p 11. (b) Hay, P. J.; Wadt, W. R. *J. Chem. Phys.* **1985**, *82*, 270. (c) Wadt, W. R.; Hay, P. J. *J. Chem. Phys.* **1985**, *82*, 284. (d) Hay, P. J.; Wadt, W. R. *J. Chem. Phys.* **1985**, *82*, 299.

(15) Frisch, M. J.; Trucks, G. W.; Schlegel, H. B.; Scuseria, G. E.; Robb, M. A.; Cheeseman, J. R.; Montgomery, J. A., Jr.; Vreven, T.; Kudin, K. N.; Burant, J. C.; Millam, J. M.; Iyengar, S. S.; Tomasi, J.; Barone, V.; Mennucci, B.; Cossi, M.; Scalmani, G.; Rega, N.; Petersson, G. A.; Nakatsuji, H.; Hada, M.; Ehara, M.; Toyota, K.; Fukuda, R.; Hasegawa, J.; Ishida, M.; Nakajima, T.; Honda, Y.; Kitao, O.; Nakai, H.; Klene, M.; Li, X.; Knox, J. E.; Hratchian, H. P.; Cross, J. B.; Bakken, V.; Adamo, C.; Jaramillo, J.; Gomperts, R.; Stratmann, R. E.; Yazyev, O.; Austin, A. J.; Cammi, R.; Pomelli, C.; Ochterski, J. W.; Ayala, P. Y.; Morokuma, K.; Voth, G. A.; Salvador, P.; Dannenberg, J. J.; Zakrzewski, V. G.; Dapprich, S.; Daniels, A. D.; Strain, M. C.; Farkas, O.; Malick, D. K.; Rabuck, A. D.; Raghavachari, K.; Foresman, J. B.; Ortiz, J. V.; Cui, Q.; Baboul, A. G.; Clifford, S.; Cioslowski, J.; Stefanov, B. B.; Liu, G.; Liashenko, A.; Piskorz, P.; Komaromi, I.; Martin, R. L.; Fox, D. J.; Keith, T.; Al-Laham, M. A.; Peng, C. Y.; Nanayakkara, A.; Challacombe, M.; Gill, P. M. W.; Johnson, B.; Chen, W.; Wong, M. W.; Gonzalez, C.; Pople, J. A. *Gaussian 03*, revision C.02; Gaussian, Inc.: Wallingford, CT, 2004.

(16) Churchill, M. R.; DeBoer, B. G. *Inorg. Chem.* **1977**, *16*, 878.

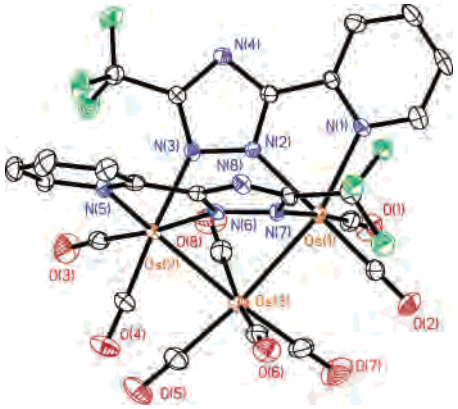

Figure 1. ORTEP diagram of **2b** with thermal ellipsoids shown at 30% probability level.

Scheme 2

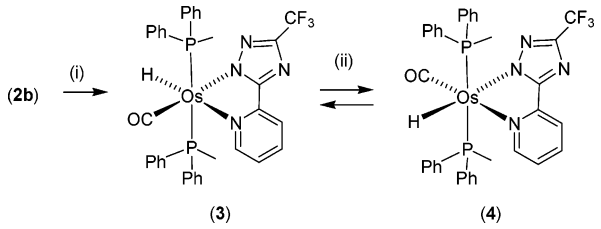

with a simple electron counting using the 18-electron rule.[17] Moreover, all osmium atoms in **2b** displayed a pseudooctahedral coordination. For the central osmium atom, the geometry is clearly defined by four carbonyl ligands and two cis-oriented Os−Os bonds. For the other osmium atoms, each is coordinated by three facially arranged nitrogen atoms deriving from the triazolate chelates. These Os−N distances varied from 2.097 to 2.222 Å, with the distances to the neutral pyridyl fragments (Os(1)−N(1) = 2.204(5) Å and Os(2)−N(5) = 2.222(5) Å) being significant longer than those to the anionic triazolate ligand distances (2.097−2.172 Å). The overall bonding arrangement associated with these multisite coordinated triazolate ligands is closely related to that found in several first-row iron(III) and copper(II) pyridyl azolate complexes.[18]

After confirming the structure of **2**, we then proceeded to investigate the chemical properties associated with these new cluster complexes. For the reactions between **2a** and fppzH (or **2b** and fptzH), the main products are the previously reported blue-emitting complexes **1a** (or **1b**) obtained by direct treatment of $Os_3(CO)_{12}$ with the pyridylazoles (Scheme 1).[10] These reactions obviously confirmed the roles of **2a**,**b** as possible reaction intermediates.

To further explore the versatile synthetic aspect of **2**, we also investigated the reactions of **2b** with excess PPh_2Me in DGME solution (Scheme 2). A simple chromatographic separation yielded a blue-emitting complex **3** and a green-emitting complex **4** in 55% and 10% of the isolated yields, respectively. Spectroscopic investigation revealed that complexes **3** and **4** were isomeric, as both possess one pyridyltriazolate chelate, one carbonyl and one terminal hydride ligand attached to the osmium(II) center, and two symmetrically arranged PPh_2Me ligands (vide infra). The source of hydride has not been confirmed, but the DGME solvent could plausibly be the major supplier. The hydride spectral pattern is consistent with this formulation in that it is coupled to two identical and strongly coupled phosphorus nuclei and thus appears as a triplet in the ^1H NMR spectra. Furthermore, heating a DGME solution of either **3** or **4** to >180 °C afforded a mixture of both complexes (see Experimental Section for the details), suggesting that these hydride complexes are interconvertible at the higher temperature. The reaction of **2a** with PPh_2Me in DGME solution displays an essentially identical result, namely the formation of two hydride isomers, and thus is not discussed here to avoid redundancy.

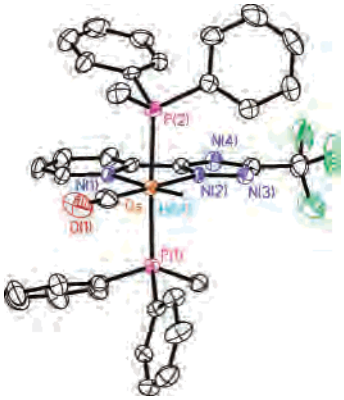

Figure 2. ORTEP diagram of **3** with thermal ellipsoids shown at 30% probability level.

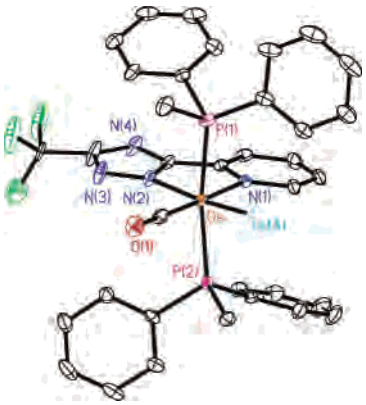

Figure 3. ORTEP diagram of **4** with thermal ellipsoids shown at 30% probability level.

Complexes **3** and **4** were further characterized through crystal structural analysis. Figures 2 and 3 reveal their molecular structures, while the metric parameters are depicted in Tables 3 and 4 for complexes **3** and **4**, respectively. The PPh_2Me ligands in both complexes adopt a trans-configuration, with Os−P distances in the range of 2.325−2.352 Å, which are comparable to that of the red-emitting Os(II)

(17) (a) Braga, D.; Sabatino, P.; Johnson, B. F. G.; Lewis, J.; Massey, A. *J. Organomet. Chem.* **1992**, *436*, 73. (b) Allen, V. E.; Mason, R.; Hitchcock, P. B. *J. Organomet. Chem.* **1977**, *140*, 297.

(18) (a) Slangen, P. M.; van Koningsbruggen, P. J.; Haasnoot, J. G.; Jansen, J.; Gorter, S.; Reedijk, J.; Kooijman, H.; Smeets, W. J. J.; Spek, A. L. *Inorg. Chim. Acta* **1993**, *212*, 289. (b) Jones, P. L.; Jeffery, J. C.; McCleverty, J. A.; Ward, M. D. *Polyhedron* **1997**, *16*, 1567. (c) Jeffery, J. C.; Jones, P. L.; Mann, K. L. V.; Psillakis, E.; McCleverty, J. A.; Ward, M. D.; White, C. M. *Chem. Commun.* **1997**, 175

Table 2. Selected Bond Lengths (Å) and Angles (deg) for Complex **2b**

Os(1)−Os(3)	2.8401(4)	Os(2)−Os(3)	2.8440(4)
Os(1)···Os(2)	3.771(1)	Os(1)−N(1)	2.204(5)
Os(1)−N(2)	2.121(5)	Os(2)−N(3)	2.167(5)
Os(2)−N(5)	2.222(5)	Os(2)−N(6)	2.097(5)
Os(1)−N(7)	2.172(5)		
Os(1)−Os(3)−Os(2)	83.127(10)	N(2)−Os(1)−N(1)	73.58(19)
N(5)−Os(2)−N(6)	73.28(19)		

Table 3. Selected Bond Lengths (Å) and Angles (deg) for Complex **3**

Os−N(1)	2.190(6)	Os−N(2)	2.127(6)
Os−P(1)	2.351(2)	Os−P(2)	2.352(2)
Os−H(1A)	1.41(7)	Os−C(1)	1.824(10)
C(1)−O(1)	1.176(11)		
P(1)−Os−P(2)	177.52(7)	N(1)−Os−N(2)	74.9(2)
N(2)−Os−C(1)	176.1(3)		

Table 4. Selected Bond Lengths (Å) and Angles (deg) for Complex **4**

Os−N(1)	2.166(3)	Os−N(2)	2.136(3)
Os−P(1)	2.3410(13)	Os−P(2)	2.3247(12)
Os−H(1A)	1.60(5)	Os−C(1)	1.835(5)
C(1)−O(1)	1.159(6)		
P(1)−Os−P(2)	168.98(4)	N(1)−Os−N(2)	74.99(14)
N(2)−Os−C(1)	101.64(17)		

complex $[Os(fppz)_2(PPh_2Me)_2]$ (2.362 Å)[19] and the corresponding porphinato (2.369 Å) and the benzotriazolato analogues (2.353 Å).[20,21] Moreover, it is notable that the pyridyl group in **3** is located trans to the strong σ-donating hydride ligand. This unique feature has caused a lengthening of the Os−N(py) distance in **3** (Os−N(1) = 2.190 Å), compared with that of its geometric isomer **4** (Os−N(1) = 2.166 Å), for which the pyridyl unit is located trans to the π-accepting CO ligand. The reverse alternation of the Os−N bond distances is also detected for the triazolate segments, indicating that the hydride is a better trans-directing ligand compared with the π-accepting CO ligand within this class of complexes. Finally, the structures of **3** and **4** are akin to that of the ionic Os(II) complexes *trans*-$[Os(diimine)(PPh_3)_2(CO)H]^+$, which are prepared by ligand substitution employing neutral diimine ligand and *mer*-$[Os(PPh_3)_3(CO)(H)Cl]$.[22]

Photophysical Properties. In addition to the geometrical isomerism, significant differences in photophysical properties were observed between **3** and **4**. Figure 4 illustrates the absorption and emission spectra of complexes **3** and **4** in cyclohexane, while Table 5 summarizes some important photophysical parameters. In general, both **3** and **4** possess nearly identical, fully allowed absorption bands in the UV region of <350 nm, for which ϵ values at the absorption maxima were calculated to be $>10^4$ M^{-1} cm^{-1} and can thus be attributed to the local $^1\pi\pi^*$ transition of the pyridine, triazolate fragment, and/or phosphine ligands. This assignment is confirmed by observation of two $^1\pi\pi^*$ bands for the parent fptz anion ($\lambda_{max} \sim 256$ and 285 nm) as well as those of the related fppz ligand reported in the literature.[10a] As for the lower lying states, the broad, structureless band at >350 nm for **3** and **4** can be tentatively assigned to a mainly, metal−ligand charge transfer (MLCT) transition in the singlet manifold. Differences in these lower lying transitions were promptly observed between **3** and **4,** in which the absorption peak of 373 nm in **3** is notably red-shifted to ~406 nm in **4**. Since the only difference between **3** and **4** is the relative orientation of CO (or H) with respect to the 2-pyridyltriazolate moiety, a possible explanation might lie in the strong π-accepting properties of CO vs the superior σ-donating behavior of the hydride ligand. On this basis, the net effect of π-acceptance from CO not only causes an electron deficiency in the Os(II) d_π orbital but also influences the moiety at the trans position, i.e., the deficiency of electron density at the triazolate and pyridyl moieties for **3** and **4**, respectively. It has been well established that, for the pyridyl triazolate chelate, the lowest intraligand transition normally incorporates the promotion of the π electron from the triazolate to the pyridyl moiety.[23] Accordingly, for the case of **3**, such a CO trans-effect should result in a decrease of the triazolate energy level and hence an increase of the triazolate → pyridyl energy gap. In similar fashion, an opposite effect is thus expected for **4** in that the π electron deficiency in the pyridyl moiety should lead to a decrease of the triazolate → pyridyl energy gap, consistent with the corresponding absorption spectral differences between **3** and **4**.

Further confirmation of the above viewpoint is provided by the theoretical approach. On the basis of TDDFT calculations, Figure 5 depicts the features of the highest occupied (HOMO) and the lowest unoccupied (LUMO) frontier orbitals of **3** and **4** mainly involved in the lower lying transition, while the descriptions and the energy gaps of each transition are listed in Table 6. In addition, the HOMO-1 orbital of **3** which plays a key role in the lowest triplet excited state (vide infra) is also shown here. As for a direct comparison of the spectral data, the lowest singlet transitions of 337 and 408 nm calculated for **3** and **4**, respectively, are in good agreement with those (**3**, 373 nm; **4**, 410 nm) obtained from the absorption spectra. The deviation of the current theoretical approach from the experimental results is not unexpected, given the underestimation of the mixing among the high-density low-lying states or the less-extensive basis set used for the Os(II) atom. Careful frontier orbital analyses conclude that the lowest singlet excitation mainly incorporates the HOMO → LUMO transition, in which the electron densities of the HOMO for **3** are mainly located at the Os(d_π) orbital, while it is simultaneously distributed over both the Os(d_π) orbital and the triazolate moiety for **4**. For the LUMO, the electron densities are mainly distributed on the pyridyl moiety of the fptz ligand in both complexes, indicating that the corresponding $S_0 \rightarrow S_1$ transition for **3** and **4** involves a pure MLCT and an ILCT/MLCT mixture,

(19) Tung, Y.-L.; Wu, P.-C.; Liu, C.-S.; Chi, Y.; Yu, J.-K.; Hu, Y.-H.; Chou, P.-T.; Peng, S.-M.; Lee, G.-H.; Tao, Y.; Carty, A. J.; Shu, C.-F.; Wu, F.-I. *Organometallics* **2004**, *23*, 3745.
(20) Xie, J.; Huang, J.-S.; Zhu, N.; Zhou, Z.-Y.; Che, C.-M. *Chem.*—Eur. J. **2005**, *11*, 2405.
(21) Olby, B. G.; Robinson, S. D.; Hursthouse, M. B.; Short, R. L. *J. Chem. Soc., Dalton Trans.* **1990**, 621.
(22) Sullivan, B. P.; Caspar, J. V.; Meyer, T. J. *Organometallics* **1984**, *3*, 1241.
(23) Chen, H.-Y.; Chi, Y.; Liu, C.-S.; Yu, J.-K.; Cheng, Y.-M.; Chen, K.-S.; Chou, P.-T.; Peng, S.-M.; Lee, G.-H.; Carty, A. J.; Yeh, S.-J.; Chen, C.-T. *Adv. Funct. Mater.* **2005**, *15*, 567.

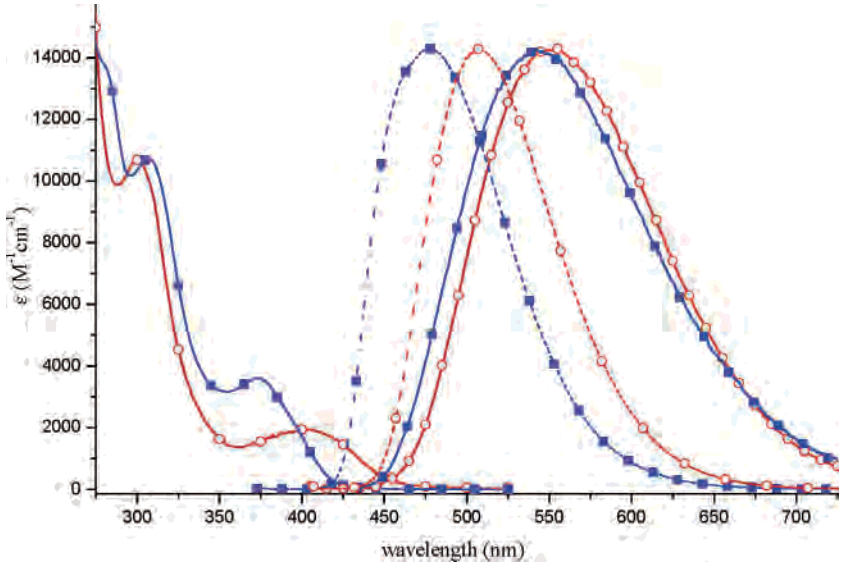

Figure 4. UV−vis absorption and normalized emission spectra of **3** (■) and **4** (○) in cyclohexane at room temperature, as well as the emission spectra of solid crystal (dashed line). Note that the emission spectra have been normalized.

Table 5. Photophysical Properties of **3** and **4** in Degassed Cyclohexane at Room Temperature

compd	abs: λ_{max} (nm) [$10^{-3}\epsilon$ (M^{-1}·cm^{-1})]	λ_{em} (nm)	τ_{em} (μs)	Φ	$10^{-4}k_r$ (s^{-1})
3	273 [14], 307 [11], 373 [3.6]	543 [475][a] (500)[b]	0.4	0.01	2.5
4	265 [27], 303 [10], 406 [2.0]	553 [510][a] (515)[b]	6.7	0.38	5.6

[a] Data in brackets were measured as thin solid film (298 K). [b] Data in parentheses were measured in 77 K methylcyclohexane.

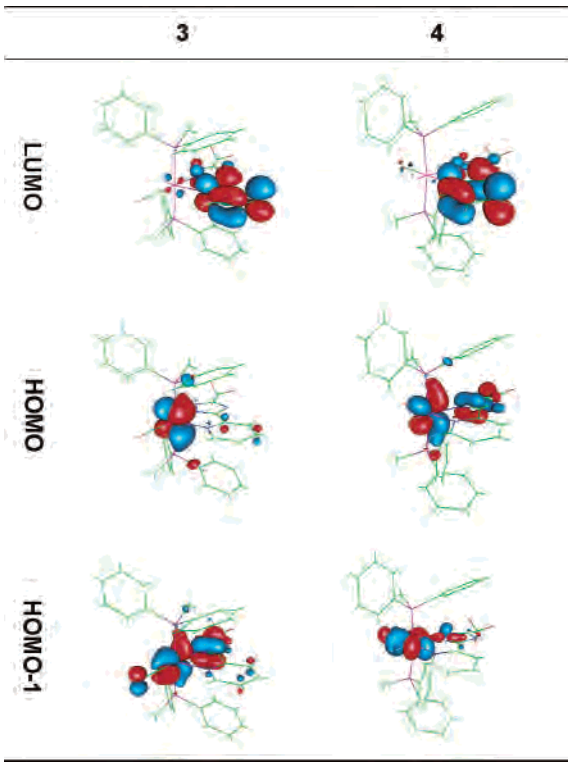

Figure 5. HOMO and LUMO of complexes **3** and **4**. Note that that the lowest lying state in both singlet and triplet manifolds is dominated by the HOMO → LUMO transition.

respectively. As for **3**, the lack of contribution from triazolate to the HOMO can be rationalized simply by its decrease in energy due to the aforementioned trans-effect raised by the π-accepting nature of CO ligand. Thus, the TDDFT approach is promising and the proposed π-accepting influence of its trans-CO moiety should play a key role in explaining the subtle differences in the S_0-S_1 absorption properties between **3** and **4**.

Despite the significant difference in the lower lying absorption spectral feature, as depicted in Figure 4, the corresponding emission profiles of **3** and **4**, with peak wavelengths at 543 and 553 nm, respectively, in cyclohexane are strikingly similar, except that the quantum efficiency in **3** (0.01 in degassed cyclohexane) is much lower than that in **4** (0.38). Both 543 nm (**3**) and 553 nm (**4**) emission bands are strongly quenched by oxygen. For example, under oxygen-free conditions, the quantum efficiency of the ~553 nm emission for **4** in cyclohexane was measured to be as high as 0.38, with a lifetime of 6.7 μs (see Table 5). Upon aeration, the corresponding quantum efficiency and lifetime were drastically reduced to 2×10^{-3} and 220 ns, respectively. For both 543 (**3**) and 553 nm (**4**) emission, the plot of decay rate versus O_2 concentration reveals a straight line (not shown here) and the O_2 quenching rate constant was deduced to be 2.1×10^9 (for **3**) and 2.3×10^9 (for **4**) M^{-1} s^{-1}, which is nearly 1/9 of the diffusion-controlled rate, consistent with a quenching mechanism that incorporates collision-induced triplet (**3** or **4**)−triplet (O_2) energy transfer. This result, in combination with the steady-state resolved large 0−0 splitting (defined as the peak-to-peak frequency between absorption and emission) of as large as ~8300 and 6500 cm^{-1} for **3** and **4**, respectively and the lack of vibronic progression feature, leads us to conclude that both 543 nm (**3**) and 553 nm (**4**) emission originates mainly from a $T_1 \rightarrow S_0$ phosphorescence, in which T_1 possesses a mixing $^3\pi\pi^*$ and ^{3}-MLCT in character. The lack of fluorescence surely guar-

Table 6. Calculated Energy Levels of the T_1 and S_1 Transitions for Complexes **3** and **4**

compd	type	λ (nm)	E (eV)	transitions	main character[a]	f
3	T_1	385.3	3.22	HOMO → LUMO (65%); HOMO-1 → LUMO (23%)	MLCT, 53.8%; ILCT, 5.3%; LLCT, 1.8%	0
	S_1	337.3	3.68	HOMO → LUMO (81%)	MLCT, 57.9%; ILCT, ≈0%	0.0209
4	T_1	449.6	2.76	HOMO → LUMO (97%)	MLCT, 50.3%; ILCT, 13.7%	0
	S_1	408.1	3.04	HOMO → LUMO (94%)	MLCT, 48.8%; ILCT, 13.2%	0.0249

[a] The main character of each transition is calculated according to the specific S_1 or T_1 excited states, while MLCT, ILCT, and LLCT represents Os(d_π) → π^*(pyridyl), π(triazolate) → π^*(pyridyl), and CO → π^*(pyridyl) transitions, respectively.

antees an ultrafast osmium-enhanced $S_1 \rightarrow T_1$ intersystem crossing rate.

A further intriguing photophysical property lies in the observation of a significant hypsochromic shift of phosphorescence for both **3** (475 nm) and **4** (510 nm) in the solid state in comparison to that in cyclohexane (see Figure 4). The possibility that the blue shift originates from crystal packing effects is very unlikely due to the octahedral geometry anchored by two bulky PPh_2Me auxiliary ligands at the trans dispositions. Further ideas regarding a rational mechanism are elaborated in the Discussion. It is however worthy of note here that the solid-state emission peak wavelength of **3** (475 nm) is located very close to the best blue-emitting iridium (III) complexes documented in the literature.[5,24]

Discussion

As shown in Table 6, the TDDFT approach also predicts an appreciably large difference in S_0-T_1 energy gap (vibronic 0−0 onset) between **3** (385 nm) and **4** (450 nm). Knowing that the absorption spectroscopy and/or TDDFT approach are strictly based on a vertical excitation, the notable difference in the absorption feature with a similar phosphorescence profile between **3** and **4** must imply a great variation in the photophysical properties for **3** (or **4**) prior to the emission. One possible explanation lies in a large dipolar change for **3** in the T_1 state (with respect to its ground state), such that a prominent solvent relaxation takes place, resulting in a significant positive phosphorescence solvatochromism,[25] of which the emission peak wavelength is coincidentally similar to that of **4**. However, the nonpolar cyclohexane used to obtain the results shown in Figure 4 casts serious doubt on this proposed mechanism. Moreover, the negligible solvent-polarity dependent emission for **3** from cyclohexane (543 nm) to CH_3CN (552 nm) further undermines this proposal. In yet another approach, a photolysis experiment has been performed for both **3** and **4** in cyclohexane upon 355 nm excitation (3rd harmonic of Nd:YAG, 10 mJ/cm^2, 10 Hz). Within a photolysis period of 30 min, negligible spectral changes were observed in both absorption and emission for complexes **3** and **4**, eliminating the possibility of photoisomerization, i.e., interconversion, between **3** and **4** in the excited state.

Knowing that the above spectral differences rely on absorption and emission in singlet and triplet manifolds, respectively, one plausible rationalization may lie in the fact that there exists an intrinsic difference in the orbital configuration between singlet (S_1) and triplet (T_1) states. As such, theoretical approaches may provide a possible clue to unravel the enigma. As depicted in Figure 5 and Table 6, in sharp contrast to a pure MLCT excited-state incorporating the HOMO → LUMO transition for the S_1 state, the respective T_1 state in **3** mainly consists of mixed HOMO → LUMO and HOMO-1 → LUMO transitions, in which the T_1 state is composed of an appreciable portion (1.8%) of CO → π^*-(pyridyl) of LLCT character (see Figure 5 and Table 6). After the photoexcitation, the deficiency of the CO π-character greatly reduces the π-accepting strength, hence weakening the Os−CO bonding strength, possibly resulting in a significant distortion of the potential energy surface with respect to that of the ground state. Accordingly, a large Stokes shift (peak-to-peak) is expected between absorption (either $S_0 \rightarrow S_1$ or $S_0 \rightarrow T_1$ (if resolvable)) and phosphorescence for **3**. In sharp contrast, for **4**, as depicted in Table 6 and Figure 5, the T_1 state mainly involves the HOMO → LUMO transition, in which the contribution of CO → π^*-(pyridyl) LLCT is essentially zero, resulting in a mirror image between absorption ($S_0 \rightarrow T_1$) and phosphorescence.

On the basis of the above arguments, one might expect a weakening of Os−CO bond, for which the potential energy surface must be much shallower than that of the ground state. The great distortion between these two potential energy surfaces may facilitate surface crossing and hence the radiationless transition.[10,26] Accordingly, the corresponding motions associated with the Os−CO bond may serve as a good deactivation mode and channel into the radiationless pathways. One strong piece of spectral evidence for this proposed mechanism lies in the ∼40-fold difference of phosphorescence intensity between **3** ($\Phi_p \sim 0.01$) and **4** ($\Phi_p \sim 0.38$) in room-temperature cyclohexane solution, despite the similar magnitude of the radiative decay rates (see Table 5). We further carried out a temperature-dependent study of **3** in methylcyclohexane. As depicted in Figure 6, upon decrease of the temperature from 310 to ∼176 K, the phosphorescence intensity increased ∼10-fold accompanied by an increase of the observed decay time ($\tau_{obs} = 1/k_{obs}$) from 0.4 to 6.5 μs. Assuming that the observed decay rate obtained at 77 K (vide infra) is equivalent to $k_r + k_{nr}$, where

(24) (a) Coppo, P.; Plummer, E. A.; De Cola, L. *Chem. Commun.* **2004**, 1774. (b) Yeh, S.-J.; Wu, W.-C.; Chen, C.-T.; Song, Y.-H.; Chi, Y.; Ho, M.-H.; Hsu, S.-F.; Chen, C.-H. *Adv. Mater.* **2005**, *17*, 285. (c) Mak, C. S. K.; Hayer, A.; Pascu, S. I.; Watkins, S. E.; Holmes, A. B.; Koehler, A.; Friend, R. H. *Chem. Commun.* **2005**, 4708. (d) Lyu, Y.-Y.; Byun, Y.; Kwon, O.; Han, E.; Jeon, W. S.; Das, R. R.; Char, K. *J. Phys. Chem. B* **2006**, *110*, 10303.

(25) (a) Farley, S. J.; Rochester, D. L.; Thompson, A. L.; Howard, J. A. K.; Williams, J. A. G. *Inorg. Chem.* **2005**, *44*, 9690. (b) Yu, J.-K.; Cheng, Y.-M.; Hu, Y.-H.; Chou, P.-T.; Chen, Y.-L.; Lee, S.-W.; Chi, Y. *J. Phys. Chem. B.* **2004**, *108*, 19908.

(26) Li, S.-W.; Cheng, Y.-M.; Yeh, Y.-S.; Hsu, C.-C.; Chou, P.-T.; Peng, S.-M.; Lee, G.-H.; Tung, Y.-L.; Wu, P.-C.; Chi, Y.; Wu, F.-I.; Shu, C.-F. *Chem.*—Eur. J. **2005**, *11*, 6347.

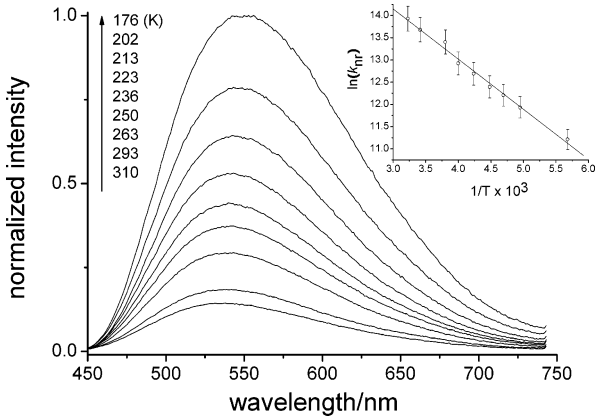

Figure 6. Temperature-dependent emission spectra of complex **3**. Insert: Linear graphical plot of ln $k_{nr}(T)$ versus $1/T$ (see text for the definition).

k_r and k_{nr} represent the radiative decay rate and temperature-independent radiationless decay rate, respectively, such that the temperature-dependent radiationless decay rate is $k_{nr}(T) = k_{obs} - (k_r + k_{nr})$, a plot of ln $k_{nr}(T)$ versus $1/T$ gives a relatively straight line (see insert of Figure 6), and the activation energy E_a for an Arrhenius-type thermally deactivated pathway was deduced to be ~2.3 kcal/mol in **3**.

It is important to note that during the temperature-dependent study of **3**, we observed a continuous increase of the emission intensity from 310 to 176 K, in which the emission spectral profile essentially remained unchanged with peak wavelength at ~533−540 nm. Interestingly, however, the spectra underwent a discrete shift to ~490 nm at 150−77 K (see Supporting Information for the spectrum obtained at 77 K). A similar spectral blue shift was observed for **4** from 553 nm at 298 K to 515 nm at <150 K in methylcyclohexane, although the emission intensity only increased by ~2-fold. The corresponding spectral profile is reminiscent of **3** and **4** in the solid crystal with 475 and 510 nm peak wavelengths, respectively. Note that 150 K is close to the freezing point of methylcyclohexane (146 K). Since the emission peak wavelength of **3** revealed negligible solvent polarity dependence, the freezing of solvent, hence the slow of the solvent relaxation, i.e., solvatochromism, to account for the spectral shift is not likely. Alternatively, we propose that certain large amplitude motions might have been locked in the solid state as well as in frozen solid solution, such that the electronic configuration alters accordingly. A prime candidate affecting this is the auxiliary phosphine ligand PPh_2Me. We herein tentatively propose that the phenyl torsional motion should affect the donor properties. In solution at 298 K, a relatively free phenyl motion can be executed, such that the electron-donating ability of PPh_2Me is averaged from these rotational motions. Once in a crystal or in a frozen form at cryogenic temperature, such motions have been restricted, i.e., locked, in a specific angle of plane for the phenyl rings, and the net effect should be quite different from that in solution phase, resulting in a subtle change of the electronic configuration. Nevertheless, one should not eliminate other possibilities, such as the rigidochromic shift[27] associated with freezing of the solvent as well as the existence of an intramolecular $\pi\pi$ interaction between a phenyl ring and the pyridyl azolate and even certain long-range, intermolecular interactions. For the latter case, an intermolecular ligand−ligand $\pi\pi$ interaction between a ligated chromophore and aryl substituted phosphine ligands has recently been reported in rhenium(I) complexes.[28]

Conclusion

In conclusion, the triosmium intermediate complexes $[Os_3(CO)_8(fppz)_2]$ (**2a**) and $[Os_3(CO)_8(fptz)_2]$ (**2b**) bearing two 2-pyridylazolate ligands have been isolated and characterized to elucidate the reaction mechanism that gives rise to the blue-emitting phosphorescent complexes $[Os(CO)_2(fppz)_2]$ (**1a**) and $[Os(CO)_2(fptz)_2]$ (**1b**). For **2b**, the reaction with the phosphine ligand PPh_2Me afforded two hitherto new hydride isomers **3** and **4**, for which the reversible interconversion was clearly established at higher temperatures (>180 °C). The subtle differences in photophysical properties between **3** and **4** have been attributed to the strong π-acceptor character of the trans CO ligand and the interplay of potential energy surfaces between S_0 and T_1 states. The results have been further supported by the frontier orbital analyses on the basis of time-dependent density function theory (TD-DFT). The results should provide a pertinent fundamental basis for the future design and preparation of highly efficient phosphorescent emitters.

Acknowledgment. This work was funded by the National Science Council of Taiwan, ROC, under Grants NSC 93-2113-M-007-012 and NSC 93-2752-M-002-002-PAE.

Supporting Information Available: CIF files for complexes **2b**, **3**, and **4** and the calculated energy levels and the associated frontier orbitals of the TDDFT calculation for complexes **3** and **4**. This material is available free of charge via the Internet at http://pubs.acs.org.

IC061301Y

(27) Colombo, M. G.; Hauser, A.; Gudel, H. U. *Top. Curr. Chem.* **1994**, *171*, 143.
(28) Tsubaki, H.; Sekine, A.; Ohashi, Y.; Koike, K.; Takeda, H.; Ishitani, O. *J. Am. Chem. Soc.* **2005**, *127*, 15544.